Evaluating the effect of oxygen vacancies

on the OER activity of LaNiO₃

Chuanmu Tian[a], Danni Wang,[a] Kelvin Hongliang Zhang,[b] and Jan P. Hofmann[a*]

[a] Surface Science Laboratory, Department of Materials- and Geosciences, Technical University of Darmstadt, Peter-Grünberg-Straße 4, 64287 Darmstadt, Germany.
[b] State Key Laboratory of Physical Chemistry of Solid Surfaces, College of Chemistry and Chemical Engineering, Xiamen University, Siming South Street 422, Xiamen 361005, P. R. China.

Corresponding author e-mail address: hofmann@surface.tu-darmstadt.de

Abstract

In this work, we have investigated the effect of oxygen vacancies on the surface composition, electronic structure and OER performance of LaNiO₃. The results show that the OER performance of LaNiO₃ can be improved both by lowering the oxygen partial pressure during film growth or annealing the thin film in H_2 atmosphere. X-ray photoemission spectroscopy (XPS) shows a significant increase in La ratio on the LaNiO₃ surface after the introduction of oxygen defects, especially after H_2 treatment where Ni/La reaches 3.5:1. The presence of oxygen vacancies leads to the aggregation of Ni on the surface of LaNiO₃, which plays a crucial role in enhancing the OER performance of LaNiO₃. In addition, the OER activity of both LaNiO₃ and oxygen vacancy rich LaNiO₃ decreases upon cyclic voltammetry (CV) between +1.0 V and +1.5 V vs. RHE with proceeding cycle numbers. XPS results reveal that the CV treatments lead to the decrease of Ni concentration at the LaNiO₃ surface, which is an important factor for the decrease in the OER performance of LaNiO₃ as well as oxygen vacancy rich LaNiO₃.

Keywords: LaNiO₃, oxygen evolution reaction, electronic structure, oxygen vacancies

Introduction

Electrochemical water splitting provides a promising pathway for storing renewable energy in chemical bonds and will contribute to solving global energy and environmental issues.[1,2] The whole process can be divided into two half-reactions, hydrogen evolution reaction (HER) and oxygen evolution reaction (OER).[3] The bottleneck for the overall water electrolysis is the OER due to the higher overpotential caused by the kinetically demanding four electron/proton transfer process.[4,5] Currently, IrO_2- and RuO_2-based catalysts have shown excellent OER activity in acidic media and have been regarded as the most promising commercial OER catalysts for proton exchange membrane (PEM) electrolysis, but their scarcity and high cost hinder their large-scale application.[6-8] As a consequence, the development of cheap, highly active and stable earth-abundant transition-metal oxides metal OER electrocatalysts is critical to water electrolysis, especially Fe, Co and Ni, when alkaline water electrolysis is considered.[9-12]

Among them, the perovskite oxides have attracted great attention due to their low cost and flexible structure properties.[13,14] Perovskite oxides have the general formula ABO_3, where A is an alkaline earth metal cation (La, Ba, Sr, etc.) and B is a transition metal cation (Fe, Co, Ni, etc.).[15] $LaNiO_3$ (LNO), a typical perovskite oxide, has attracted much attention due to its excellent OER activity and adjustable electronic structure.[16-18] Over the past decades, different strategies have been explored to enhance the electrochemical activity of LNO, including nanostructure engineering, aliovalent doping and the introduction of oxygen vacancies.[19-22] Recently, Thomas and his co-workers reported that annealing LNO in H_2 atmosphere can induce oxygen vacancies at the LNO surface, leading to a significant enhancement in OER activity and stability of LNO.[23] They attributed the enhanced LNO OER performance to oxygen vacancies which promote electrical conductivity. Later, Sun et al. found that doping by Ce can significantly improve the OER performance of $LaNiO_3$.[24] They argue that Ce doping can introduce oxygen vacancies in LNO, which promote the conversion of Ni to a NiOOH surface phase during the OER process and thus increase the OER activity. The

2

NiOOH surface phase being the catalytically active phase of the material. Additionally, it has been reported that LNO electrocatalysts usually undergo surface morphology and compositional changes during OER process.[25-28] Liu et al. reported that the deposition of LNO particles on LNO films can significantly improve the OER activity of LNO films.[29] They attributed the enhancement of OER activity to the fact that the particles on the surface of LNO are reconstructed to form NiOOH active species during the OER process. Later, Sun and coworkers have been directly observing the surface reconstruction process of $LaNiO_3$ thin film during the OER by using electrochemical-scanning tunneling microscopy (EC-STM).[30] So far, there have been many studies on the effect of oxygen vacancies on the OER performance of LNO. However, the relationship between oxygen vacancy on the surface chemical composition, electronic structure and the OER activity of LNO has not been systematically investigated and verified, especially by using a single crystal thin film model system.

In this work, in order to establish a relationship between the surface properties, i.e., active surface phase composition and electronic structure, and the OER activity of the LNO with oxygen vacancy, we have employed epitaxial $LaNiO_3$ (001) single crystalline films as models to exclude the effect of nanostructure. We prepared a series of well-defined $LaNiO_3$ single crystal films on Nb-doped $SrTiO_3$ (001) substrate by using a pulsed laser deposition (PLD) method. At the same time, we used two different ways to introduce oxygen defects in LNO and investigated the effect of oxygen vacancies on OER activity and stability. In addition, the surface composition and electronic structure before and after OER treatment were characterized by XPS. The results revealed that the OER performance of LNO and LNO with oxygen vacancies highly depends on the surface Ni/La ratio.

Experimental section

Materials preparation

$LaNiO_3$ targets were synthesized by solid-phase reaction. Stoichiometric amounts of La_2O_3 (Alfa, > 99.999%) and NiO (Alfa, > 99.999%) were mixed in a mortar. After

3

grinding for 2 hours, the powder was pressed into pellets through a hydraulic press at 10 tons of pressure for 2 minutes, and finally these pellets were calcined in a muffle furnace (Kejing, KSL-1700) at 1000 °C for 24 h with a 5 °C/min heating rate, followed by naturally cooling to room temperature. $LaNiO_3$ single crystalline thin films were grown on one-side polished (100)-oriented 0.1% Nb-doped $SrTiO_3$ (HeFei, Kejing) substrates by PLD using the respective oxide targets. Laser ablation was performed at a repetition rate of 5 Hz and an energy density of 1.0 J/cm^2 with a 248 nm KrF excimer laser. To achieve ~30 nm film thicknesses, the laser was impinged on the target for 30 min applying a substrate temperature of 650 °C and an O_2 partial pressure of 13.3 Pa. We have adopted two approaches to introduce oxygen vacancies into $LaNiO_3$, one is by lower the oxygen partial pressure to 6 Pa during sample preparation by PLD. And the other was to anneal the $LaNiO_3$ thin film in a tube furnace at 350 °C for 2 h in flowing forming gas (5% H_2 and 95% Ar) with an volume flow of 300 mL/min STP.

Materials characterization

The crystal structure of the pure $Ni_xCo_{3-x}O_4$ (x = 0, 0.3, 1.0) targets was analyzed by X-ray diffraction (XRD) using Cu Kα radiation generated at 40 kV and 44 mA. Thin film growth was examined by high-resolution X-ray diffraction using a rotating Cu anode (45 kV, 190 mA) Rigaku SmartLab diffractometer in θ-2θ geometry, equipped with a Ge (220) double bounce monochromator (selecting the Cu Kα$_1$ wavelength) in parallel beam mode, while the thickness of the films was determined by X-ray reflectivity (XRR) scans on the SmartLab diffractometer. The surface morphologies of the $LaNiO_3$ sample before and after OER treatments were determined by atomic force microscopy (AFM) with Bruker Icon Dimension AFM in amplitude modulation mode using PPP-Zeihr cantilevers (NanoAndMore GmbH, Wetzlar, Germany). This type of cantilever has a nominal spring constant of 27 N/m, a nominal resonance frequency of 130 kHz, and a typical tip radius of <7 nm. The free oscillation amplitude of the cantilever tip was adjusted to $A_0 \approx 120$ nm, and a setpoint ratio of $A_{sp}/A_0 \approx 0.7$ was set to ensure operation in the repulsive tip–sample interaction regime. We scanned the surface with a tip

4

velocity of 2 μm/s.

The X-ray photoelectron spectroscopy (XPS) was performed with a hemispherical energy analyzer (PHOIBOS 150, Focus 500 with XR50M) at a pressure $<10^{-9}$ mbar and monochromatized Al Kα radiation (1486.74 eV) was utilized for excitation. Survey spectra were recorded with a pass energy of 20 eV and detailed spectra were recorded at 10 eV. The system was calibrated to 0.00 eV binding energy of the Fermi level by the core lines of copper, silver, and gold as well as to the emission lines of Au $4f_{7/2}$ at 83.98 eV, Ag $3d_{5/2}$ at 368.26 eV, and Cu $2p_{3/2}$ at 932.67 eV binding energy with deviations ≤0.1 eV.[31] The data was analyzed with CasaXPS, version 2.3.24. The spectra were fitted with Shirley background and peaks are fitted with GL (30) lineshapes.

Electrochemical measurements were carried out in a three-electrode configuration using a Gamry electrochemical workstation (Interface 1000E) setup in PECC-2 cell from Zahner Elektrik GmbH & Co. KG. A platinum wire was used as a counter electrode and Hg/HgO (1 M KOH) as a reference electrode. All measurements werere carried out in purified 1 M KOH. Before measurements, the Hg/HgO was calibrated by an SHE (HydroFlex, Gaskatel). The cyclic voltammetry (CV) measurements were performed in 1 M KOH at a scan rate of 100 mV/s with the potential from +1.0 to +1.5 V (vs. RHE) were used to activate thin films. Each sample was subjected to four OER activation processes, namely 10 CV, 200 CV, 500 CV, and 1000 CV. After each activation process, we carried out additional 5 CVs between +1.0 V to +1.8 V vs RHE to obtain the OER performance of the film. Electrochemical impedance spectroscopy (EIS) tests were measured at a potential of +1.7 V (vs RHE) within the frequency range of 100 kHz to 1 Hz. The electrochemically active surface area (ECSA) was determined by double-layer capacitance measurements.[32] Specifically, testing CV in the non-Faradaic region around +1.10 V vs at different scan rates (0.01, 0.02, 0.04, 0.06, 0.08, 0.10, 0.20, and 0.30 V s^{-1}).

5

Results discussion

Structural characterization

The XRD patterns of LNO, LNO-V_o and LNO-V_o' are shown in Figure 1. The peak at $2\theta = 46.4°$ corresponds to the (002) orientation of the 0.1% Nb-doped $SrTiO_3$ single crystal substrate, while the peaks at 47.8°, 47.6° and 47.5° correspond to (002) oriented LNO, LNO-V_o and LNO-V_o', respectively. Well-defined oscillations are observed in both XRD and XRR plots for LNO, LNO-V_o, indicating high quality of these thin films. However, the disappearance of oscillations in LNO-V_o' oscillation means that the H_2 treatment results in the film having lost its epitaxial relation to the substrate. It can be seen that the peak position of LNO shifted to lower angles when oxygen vacancies were introduced. The corresponding lattice constants are displayed in Figure 1b. The lattice constants of LNO are 3.802 Å, while the lattice constants of LNO-V_o and LNO-V_o' are 3.810 Å and 3.815 Å. It can be observed that the lattice constant increases when oxygen vacancies are introduced in LNO, a phenomenon also observed for other perovskites such as$BaTiO_3$.[33] The increase in lattice constant can be attributed to the introduction of oxygen defects resulting in the reduction of Ni^{3+} to Ni^{2+}, and the ionic radius of Ni^{2+} is larger than that of Ni^{3+}, which in turn leads to an increase in lattice constant. In addition, we also noticed that the peak intensity of both LNO-V_o and LNO-V_o' decreases, indicating that the introduction of oxygen vacancies leads to a decrease in the crystallinity of the sample. The decrease in crystallinity of LNO-V_o' is particularly pronounced, suggesting that the H_2 treatment resulted in a severe alteration of the film surface, which is further confirmed by the following AFM results.
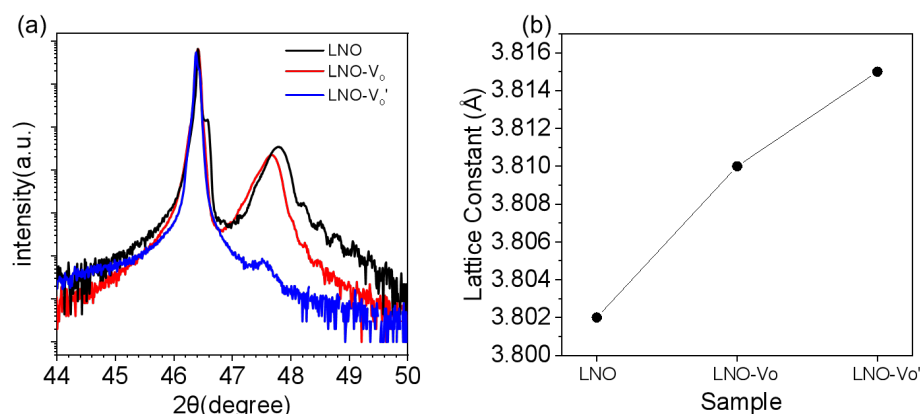
Figure 1. (a) XRD pattern of LNO (black), LNO-V_o (red), LNO-V_o' (blue) and (b) the corresponding lattice constants.

Surface Morphology

The surface morphology of LNO, LNO-V_o and LNO-V_o' was characterized by AFM. As shown in Figure 2a, the root mean square roughness (RMS) of LNO is 3.75 nm, while the RSM of LNO-V_o (Figure 2b) and LNO-V_o' (Figure 2c) is 4.14 nm and 0.85 nm, respectively. This variation shows that introducing oxygen vacancies by controlling the partial pressure of oxygen during film growth led to an increase in the RSM of the films, while the particle size and morphology of LNO-V_o (Figure 2e) did not change significantly compared to those of LNO (Figure 2d). The increased RSM of LNO-V_o is due to the appearance of oxygen vacancies during sample preparation, which has been also observed in ZnO epitaxial thin films.[34] However, introducing oxygen vacancies by H_2 annealing led to a significant decrease in the RSM of the films (Figure 2c). The decrease of RSM of LNO-V_o' is attributed to the reorganization of the surface during the H_2 annealing process. More importantly, the AFM 3D images reveal that the LNO-V_o' (Figure 2f) samples show a more pronounced island structure compared to LNO (Figure 2d) and LNO-V_o (Figure 2e), attributed to the H_2 treatment leading to the reorganization of the LNO surface.
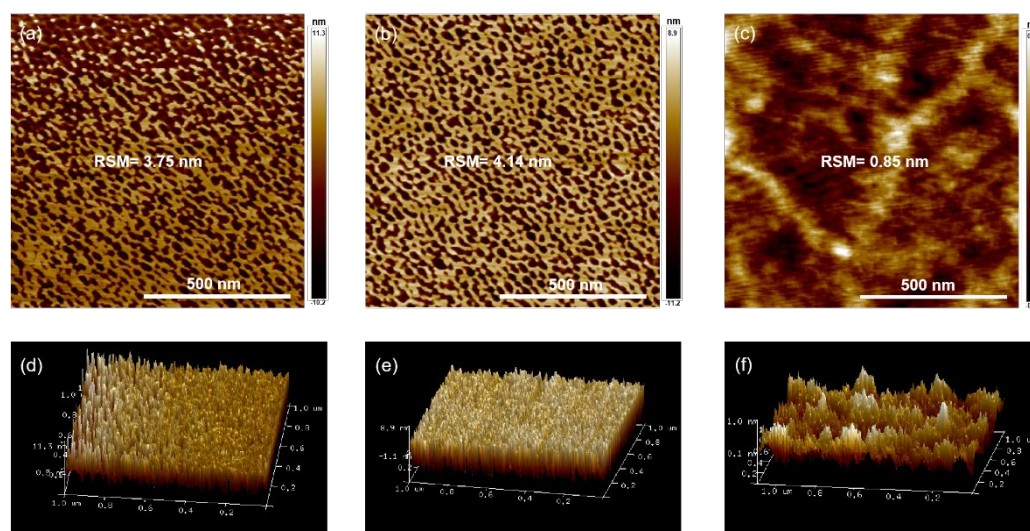
7

Figure 2. AFM results of LNO with different oxygen vacancy. (a) LNO 2D image, (b) LNO-V_o 2D image, (c) LNO-V_o' 2D image, (d) LNO 3D image, (e) LNO-V_o 3D image and (f) LNO-V_o' 3D image.

Surface Composition

Lab-based XPS measurements were carried out to investigate the chemical composition and electronic structure of LNO with different amounts of oxygen vacancies. The XPS core-level spectra were used to investigate the chemical state and surface composition of the prepared thin film samples. Since the Ni $2p_{3/2}$ is overlapping with La $3d_{3/2}$, we used the Ni 3p region to calculate the ratio of Ni^{2+} to Ni^{3+}. Figure 3 shows the high-resolution Ni 3p and La $3d_{5/2}$ spectra of LNO, LNO-V_o and LNO-V_o'. The peak components in Figure 3a at 66.4 eV (A) and 68.3 eV (B) correspond to Ni^{3+} $3p_{3/2}$ and Ni^{3+} $3p_{1/2}$, while the peaks at 70.0 eV (C) and 71.9 eV (D) can be assigned to Ni^{2+} $3p_{3/2}$ and Ni^{2+} $3p_{1/2}$.[35] The spin-orbit splitting distance between Ni $3p_{3/2}$ and Ni $3p_{1/2}$ for Ni^{2+} and Ni^{3+} is 1.9 eV, which is close to the theoretical value of 2 eV.[36] The area of the fitted components of the Ni 3p region was employed to determine the ratio of Ni^{2+} and Ni^{3+}, reported in Table 1. The results show that introducing oxygen defects in LNO in different ways leads to a decrease in Ni^{3+} concentration. It is well known that oxygen vacancies induce n-type doping, resulting in extra electrons in the system, which further reduces the Ni^{3+} to Ni^{2+}. Therefore, the concentration of Ni^{3+} in LNO decreases when oxygen vacancies exist in the LNO. In addition, the concentration of Ni^{2+} is higher in LNO-V_o' than LNO-V_o, which indicates a higher concentration of surface oxygen

8

vacancies in LNO-V_o'. The fitting peaks in La $3d_{5/2}$ show that there are two species of La$_2$O$_3$ and La(OH)$_3$ in all LNO samples, where I corresponds to La$_2$O$_3$, II corresponds to La(OH)$_3$, and III and IV correspond to the satellite peaks of La$_2$O$_3$ and La(OH)$_3$.[37] The surface composition ratios of Ni^{2+}/Ni^{3+} and Ni/La are shown in Table 1. In addition, the O 1s spectra of LNO, LNO-V_o and LNO-V_o' are shown in Figure 4. There are three species in the O 1s spectra, namely lattice oxygen (A), adsorbed hydroxyl (B) and adsorbed water (C).[38] The results show that the intensity lattice oxygen peak (A) decreased in the LNO-V_o and LNO-V_o' compared to the LNO, which is attributed to the oxygen vacancy. More importantly, the intensity of lattice oxygen in the LNO-V_o' is much lower than in LNO-V_o, which indicates that the H$_2$ annealing process produces more oxygen vacancies on the surface of the thin film samples. The more oxygen vacancies in LNO-V_o' is consistent with the higher Ni^{2+} concentration shown in Table1.

Table 1 XPS-derived atomic ratio of Ni^{2+}/Ni^{3+} and Ni/La in LNO, LNO-V_o and LNO-V_o'.

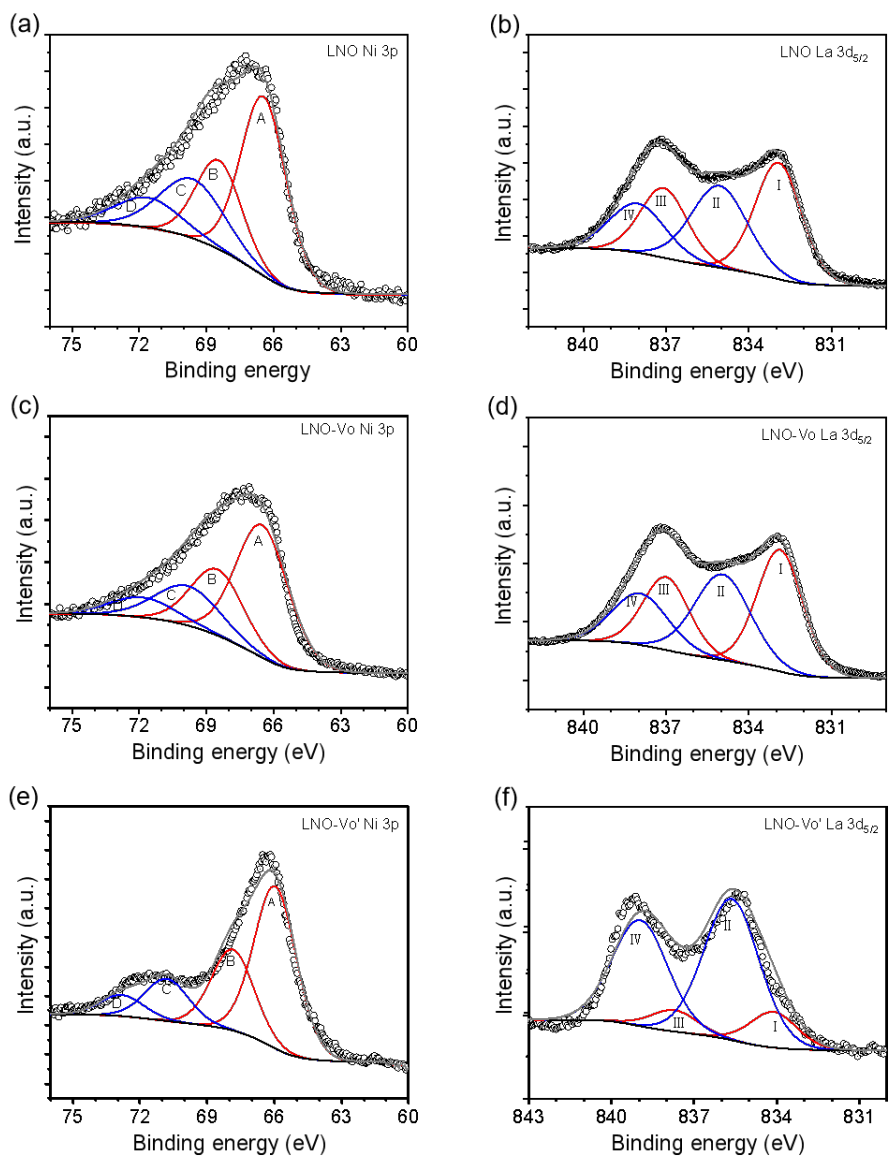| Sample	Ni^{3+} (%)	Ni^{2+} (%)	Ni^{2+}/Ni^{3+}	Ni/La
LNO	31.8	68.2	1:2.1	0.86:1
LNO-V_o	27.0	73.0	1:2.7	0.92:1
LNO-V_o'	21.0	79.0	1:3.8	3.5:1

Figure 3. Ni 3p and La $3d_{5/2}$ XPS spectra. (a) Ni 3p of LNO, (b) La $3d_{5/2}$ of LNO, (c) Ni 3p of LNO-V_o, (d) La $3d_{5/2}$ of LNO-V_o, (e) Ni 3p of LNO-V_o' and (f) La $3d_{5/2}$ of LNO-V_o'.
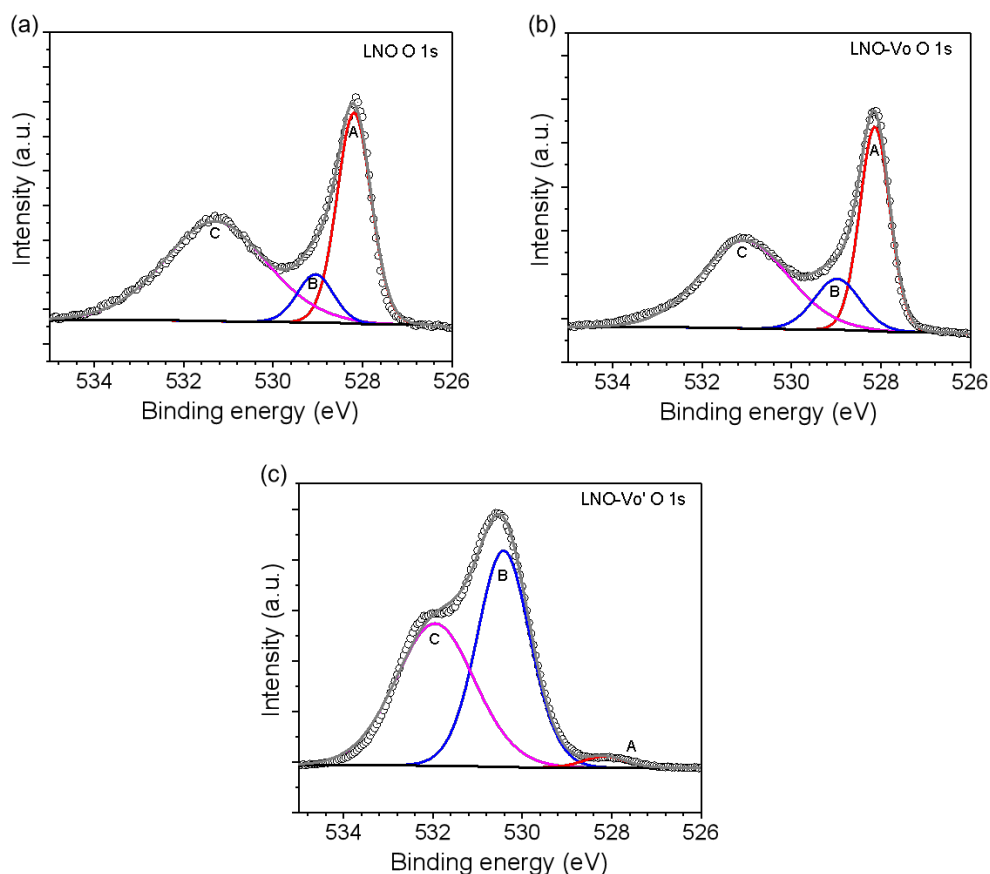
Figure 4. O 1s XPS spectra. (a) O 1s of LNO, (b) O 1s of LNO-V_o, (c) O 1s of LNO-V_o'.

OER Performance

The OER performance of LNO, LNO-V_o and LNO-V_o' was evaluated in 1 M KOH by cyclic voltammetry with a scan rate of 10 mV/s. In order to eliminate the influence of Fe impurities in KOH electrolyte on the performance of OER, the KOH electrolyte that we used has been purified.[39] Figure 5a shows the CV plot of LNO, LNO-V_o and LNO-V_o' after 10 CV cycles of the activation process with the potential ranging from +1.0 to +1.5 V vs RHE. The potential is iR compensated by solution resistance. It shows that introducing of oxygen vacancies in the LNO can enhance the OER performance, which is consistent with previous studies.[23,24] In addition, we note that the OER performance of LNO-V_o' is much higher than that of LNO-V_o, which is attributed to the higher concentration of oxygen defects in LNO-V_o' as shown in the above XPS results. Meanwhile, we also noted that oxygen vacancies affect the Ni/La ratio on the film surface. The XPS La 3d and Ni 3p spectra (Figure 3 and Table 1) show that the ratio of

11

Ni/La reaches 3.5:1 in LNO-V_o' while it is only 0.92:1 in LNO-V_o, indicating the formation of a Ni-rich surface when annealing the LNO in the H_2 atmosphere. The nickel-rich surface is also another important factor contributing to the superior OER performance of LNO-V_o'. More importantly, since the surface roughness and the morphology of the samples change after introduction of oxygen defects as observed in the AFM results, the morphology significantly affects the OER activity. To eliminate the influence of morphological change on the OER performance, we normalized the current density of the CV plots by using the electrochemical active surface area (ECSA), as shown in Figure 5b. The results showed that introducing oxygen defects was still beneficial to the activity of OER when normalizing the current on the ECSA. We also carried out EIS measurements to investigate the charge transfer at the solid-liquid interface. Figure 5d shows the Nyquist plots of LNO, LNO-V_o and LNO-V_o' at a potential of +1.7 V (vs RHE). The Nyquist plots are simulated by the Randles equivalent circuit, the fitted values of charge transfers resistance (R_{ct}) are summarized in Table 2. The R_{ct} of LNO-V_o and LNO-V_o' is much smaller than that of LNO, indicating oxygen vacancy can facilitate the charge transfer process at LNO and electrolyte interface.

Table 2 Fitted R_{ct} values of LNO, LNO-V_o and LNO-V_o'

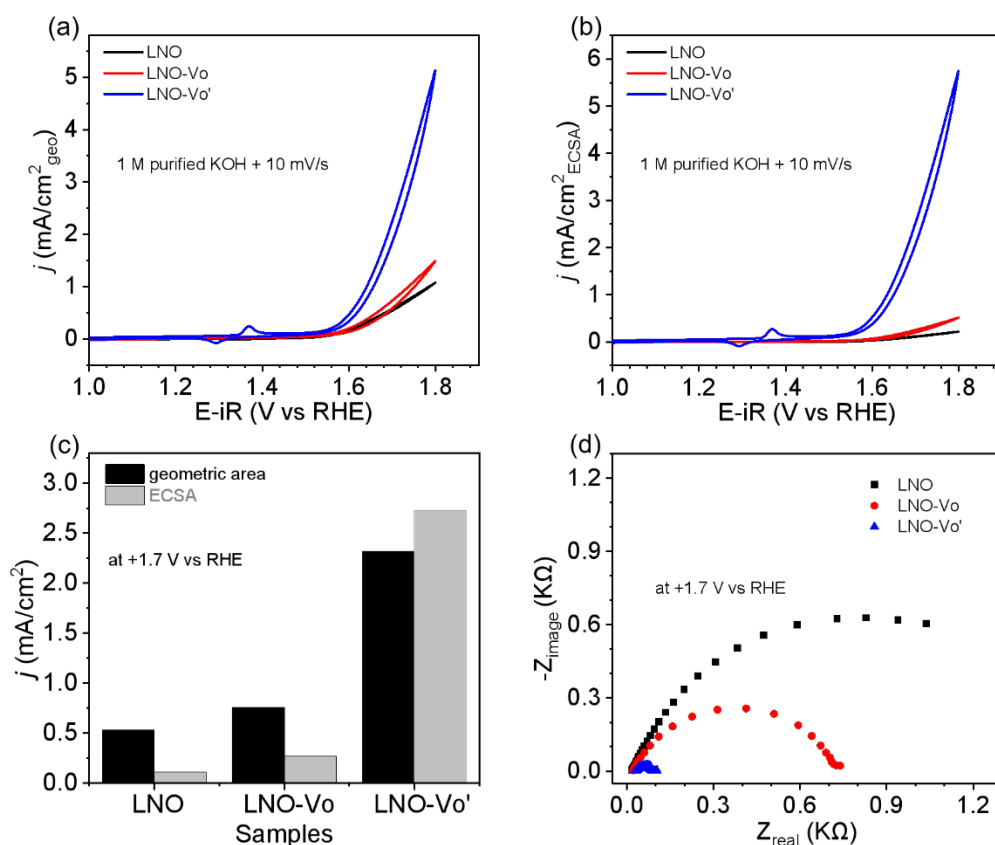| Sample	LNO	LNO-V_o	LNO-V_o'
R_{ct} (kΩ)	0.82	0.36	0.06

Figure 5. (a) CV polarization plot of LNO, LNO-V_o and LNO-V_o' with the current density normalized by geometric area. (b) CV plot of LNO, LNO-V_o and LNO-V_o' with the current density normalized by ECSA. (c)Current density of LNO, LNO-V_o and LNO-V_o' normalized by different areas at +1.7 V (vs RHE) and (d) Nyquist plot of LNO (black), LNO-V_o (red) and LNO-V_o' (blue) measured at +1.7 V (vs RHE). The smaller semicircle indicates a faster change transfer rate.

Next to activity, stability is aso an important metric for evaluating OER performance of a catalyst material. We measure the CV polarization plot after 10 CV and 1000 CV cycles with the potential range of +1.0 V to 1.5 V vs RHE at 100 mV/s scan rate, as shown in Figure 6. To evaluate the stability of the catalysts, we measured the current density at +1.7 V vs RHE (Figure 6d) after the cycling treatment. The current density of LNO at +1.7 V vs RHE decreases from 0.53 mA/cm^2 (10th CV) to 0.45 mA/cm^2 (1000th CV), LNO-V_o decreases from 0.76 mA/cm^2 to 0.50 mA/cm^2, while LNO-V_o' decreases from 2.31 mA/cm^2 (3rd CV) to 1.17 mA/cm^2 (30th CV) - a reduction of 15%,

13

34% and 49%, respectively. LNO shows lower degradation in the OER activity compared to the other two samples containing oxygen vacancies. In addition, the degradation of LNO-V$_o$' is particularly severe, and the OER performance drops to almost half after 1000 CV.
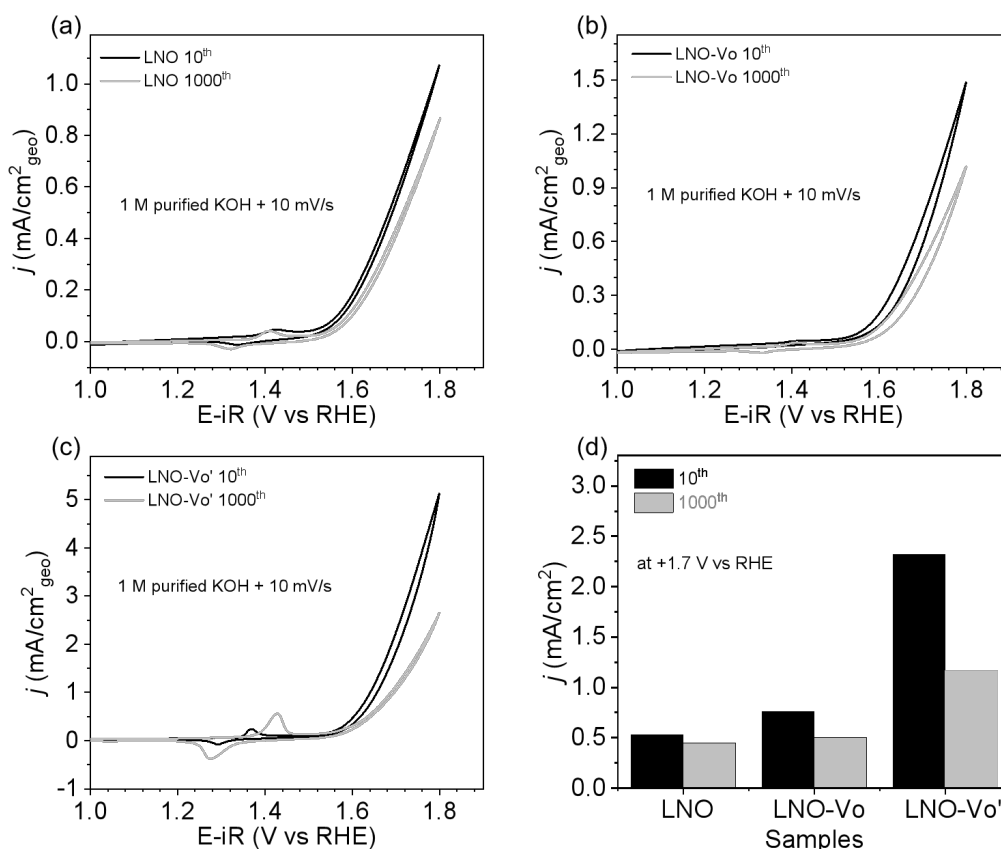

Figure 6. CV polarization profiles after 10 CV cycles and 1000 CV cycles between 1.0 to 1.5 V vs RHE. (a) LNO, (b) LNO-V$_o$, (c) LNO-V$_o$' and (d) the current density after different CV cycles at +1.7 V (vs RHE).

Characterization after OER treatment

Phase Characterization

The XRD measurements performed after 1000 CV were used to investigate the effect of electrochemical treatment on the crystallinity of those thin films, the results are shown in Figure 7. The data show that the peak intensity of the (002)-peak of the LNO (Figure 7a) film decreased after 1000 CV cycles, allowing the assumption that OER electrochemical treatment leads to a deterioration of film crystallinity. The weakening

14

of the XRD diffraction peak intensity after OER treatment is attributed to the surface reconstruction of the LNO surface and bulk structure with OER cycling, which has been observed for LNO in previous reports.[24] In addition, the peak position of LNO after 1000 CV shifts from 47.8° to 47.6 after 1000 CV, which indicates that the lattice constant of the thin film increased from 7.68 Å (a = b = c = 8.173 Å) to 7.71 Å (a = b = c = 8.187 Å) due to surface reconstruction during the OER process. The weaker peak intensity was also observed in LNO-V_o (Figure 7b) and LNO-V_o' (Figure 7c) after 1000 CV, but the peak position kept constant.
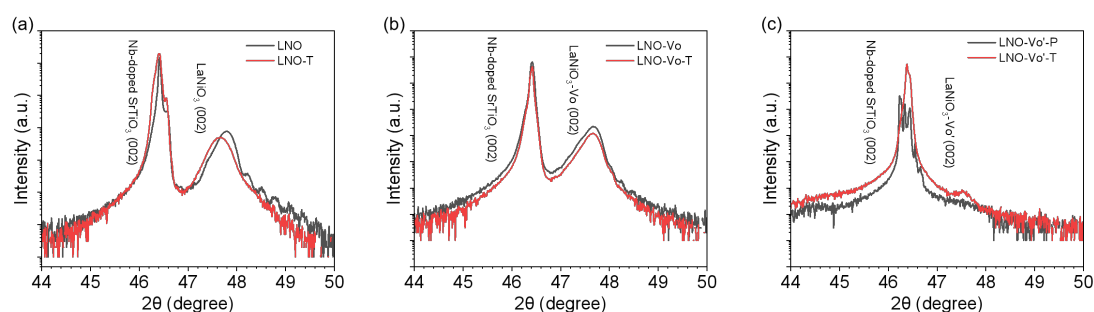

Figure 7. XRD plots before (black line) and after 1000 CV cycles (red line). (a) LNO, (b) LNO-V_o and (c) LNO-V_o'.

Surface Morphology

To investigate the effect of electrochemical treatments on the surface morphology of the different thin films, we carried out AFM measurements for LNO, LNO-V_o and LNO-V_o' after 1000 CV cycles, the results are shown in Figure 8. After 1000 CV, the RSM of LNO decreased from 3.75 nm (Fig. 2a) to 1.97 nm (Figure 8a), the RSM of LNO-V_o decreased from 4.14 nm to 1.98 nm, while the RSM of LNO-V_o' increased from 0.85 nm to 2.65 nm. The change in RMS of LNO, LNO-V_o and LNO-V_o' after 1000 CV cycles can be most likely ascribed to surface reconstruction of those thin film with OER cycling and is in good accordance with the XRD results (Figure 7). The influence of OER treatment on the surface properties of LNO, LNO-V_o and LNO-V_o' films can be further observed in the corresponding AFM 3D images in Figure 8. Among them, the changes in the LNO-V_o' film due to OER treatment were most pronounced. Overall, the surface reconstruction with OER cycling leads to change in the roughness and particle size of all thin films.
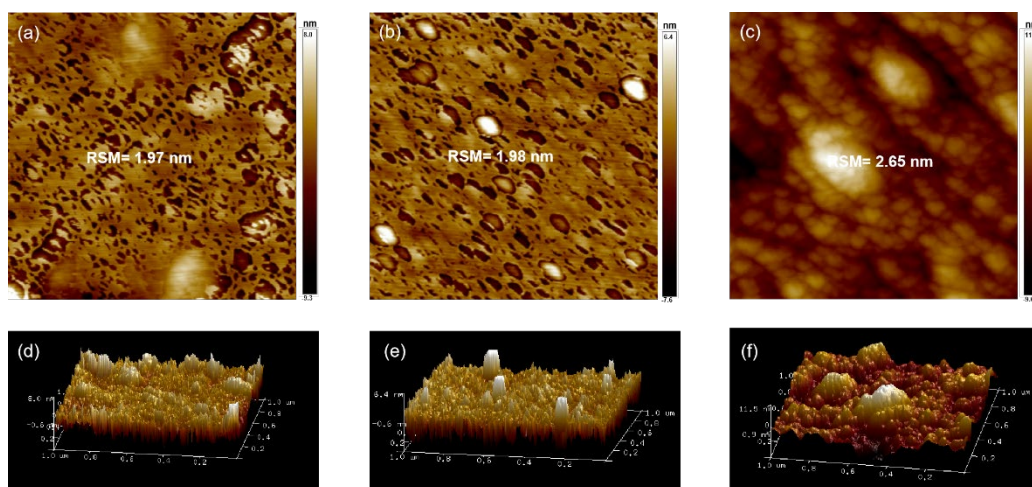
Figure 8. AFM result after 1000 CV cycles. (a) LNO-T 2D image, (b) LNO-V_o-T 2D image, (c) LNO-V_o'-T 2D image, (d) LNO-T 3D image, (e) LNO-V_o-T 3D image and (f) LNO-V_o'-T 3D image.

Surface Composition

In order to obtain a more in-depth understanding of OER stability of LNO, LNO-V_o and LNO-V_o', we measured the high-resolution Ni 3p and La 3d spectra after 1000 CV cycles, as shown in Figure 9. The surface compositions of Ni^{2+}/Ni^{3+} and Ni/La from XPS results after 1000 CV cycles are shown in Table 3, revealing that the ratio of Ni/La in LNO, LNO-V_o and LNO-V_o' decreased after 1000 CV cycles, indicating Ni concentration on the surface for all samples decreased. Specifically, the Ni/La ratio after 1000 CV decreased from 0.86:1 to 0.7:1 in LNO, 0.92:1 to 0.76:1 in LNO-V_o and 3.5:1 to 2.7:1 in LNO-V_o'. Thus, we attribute the decrease in OER activity of LNO, LNO-V_o and LNO-V_o' after 1000 CV to the decline in surface Ni concentration. In addition, we also noticed that the decrease in Ni/La ratio in LNO-V_o' after 1000 CV was particularly pronounced compared to LNO and LNO-V_o, which is consistent with the most severe attenuation of OER activity in LNO-V_o'.
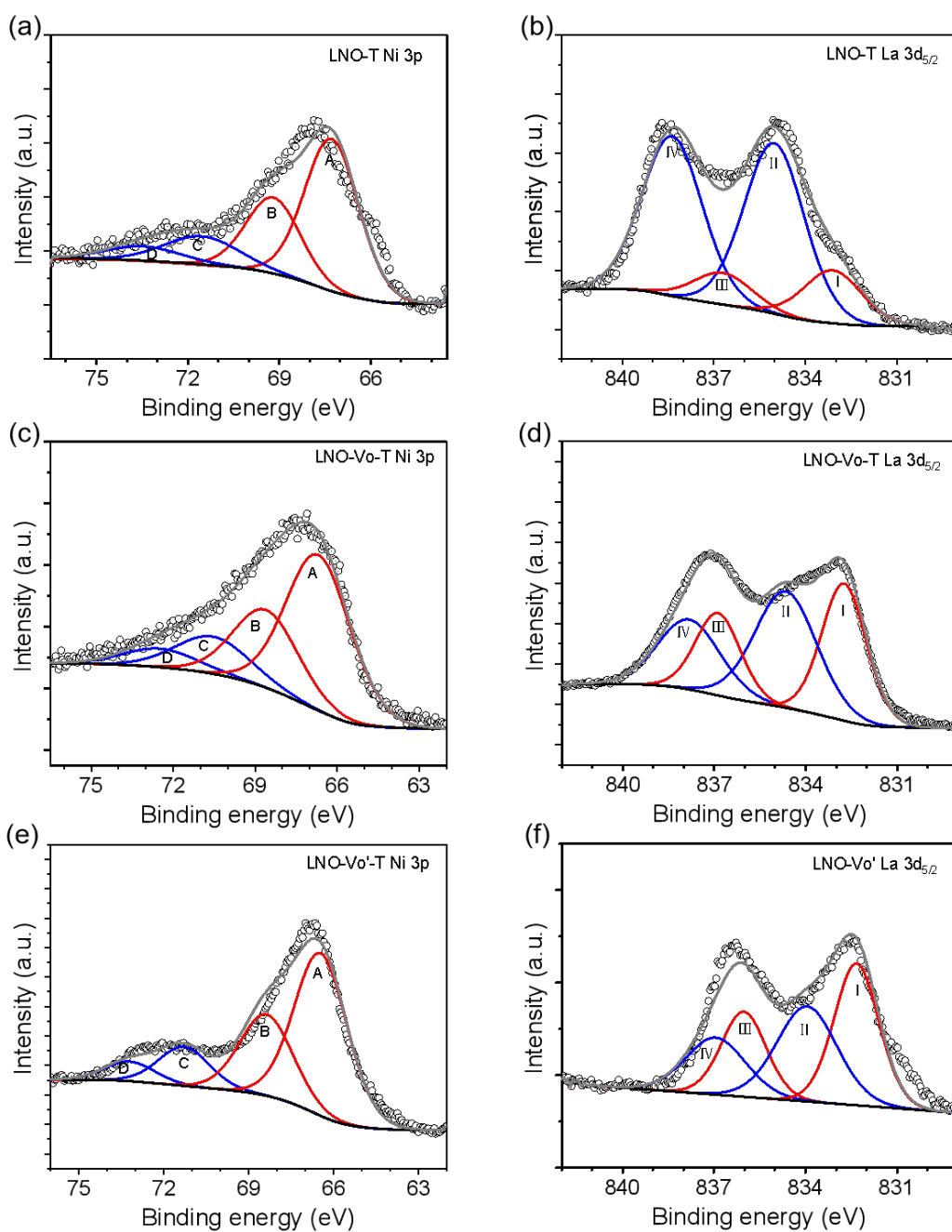
16

Figure 9. XPS Ni 3p and La $3d_{5/2}$ spectra after 1000 CV cycles. (a) Ni 3p of LNO, (b) La $3_{d5/2}$ of LNO, (c) Ni 3p of LNO-V_o, (d) La $3d_{5/2}$ of LNO-V_o, (e) Ni 3p of LNO-V_o' and (f) La $3d_{5/2}$ of LNO-V_o'.

Table 3 XPS-derived ratio of Ni^{2+}/Ni^{3+} and Ni/La in LNO, LNO-V_o and LNO-V_o' after 1000 CV cycles.

Sample	Ni^{3+} (%)	Ni^{2+} (%)	Ni^{2+}/N^{3+}	Ni/La

LNO-T	18.9	81.1	1:4.3	0.7:1
LNO-V_o-T	21.6	78.4	1:3.6	0.76:1
LNO-V_o'-T	18.5	81.5	1:4.4	2.7:1

Conclusion

Single-crystalline LNO films were used as a model system to investigate the effect of oxygen vacancies on the electronic structure and OER activity of LNO. We used two ways to introduce oxygen vacancies in LNO, i.e., by i) lowering the oxygen partial pressure during PLD preparation of the film and ii) annealing LNO in H_2. The results show that the introduction of oxygen vacancies in both ways can increase the OER activity of LNO, with the H_2 annealing treatment delivering the largest effect. XPS results reveal that oxygen defects lead to the aggregation of Ni to the surface of the samples, especially in LNO-V_o' where the Ni/La ratio reaches 3.5:1. The observed oxygen vacancies accompanied with the aggregation of Ni at the surface of LNO-V_o' was evaluated to play a key role in determining OER performance. More importantly, the OER activity of LNO, LNO-V_o and LNO-V_o' decreased after 1000 CV cycles. We found that the decrease in nickel concentration on the sample surface after 1000 CV is an important factor in the decay of OER performance. Overall, our study further demonstrates the importance of investigating well-defined model systems to accurately interpret electrochemical properties in relation to electronic structure for optimized OER performance.

Acknowledgements

References

1. Sun, H. N.; Xu. X. M.; Kim, H.; Jung. W C.; Zhou, W.; Shao, Z. P. Electrochemical Water Splitting: Bridging the Gaps Between Fundamental Research and Industrial Applications. *Energy Environ. Mater.* **2023,** *6,* 12441.

2. Li, L. G.; Wang, P. T.; Shao, Q.; Huang, X. Q. Metallic Nanostructures with Low Dimensionality for Electrochemical Water Splitting. *Chem, Soc. Rev.* **2020,** *49,* 3072-3106.

3. Gorlin, Y.; Jaramillo, T. F. A Bifunctional Nonprecious Metal Catalyst for Oxygen Reduction and Water Oxidation, *J. Am. Chem. Soc.* **2010,** *132,* 13612−13614.

4. Zhang, K. X.; Zhou, R. Q. Advanced Transition Metal-Based OER Electrocatalysts: Current Status, Opportunities, and Challenges. *Small* **2021,** *17,* 2100129.

5. Hong, W. T.; Stoerzinger, K. A.; Lee, Y. L.; Giordano, L.; Grimaud, A.; Johnson; A. M.; Hwang. J.; Crumlin, E. J.; Yang, W. L.; Shao-horn, Y. Charge-Transfer-Energy-Dependent Oxygen Evolution Reaction Mechanisms for Perovskite Oxides. *Energy Environ. Sci.* **2017,** *10,* 2190-2200.

6. Li, L.; Wang, B.; Zhang, G. W.; Yang, G.; Yang, T.; Yang, S.; Yang, S. C. Electrochemically Modifying the Electronic Structure of IrO_2 Nanoparticles for Overall Electrochemical Water Splitting with Extensive Adaptability. *Adv. Energy. Mater.* **2020,** *10,* 2001600.

7. Zagalskaya, A.; Alexandrov, V. Role of Defects in the Interplay between Adsorbate Evolving and Lattice Oxygen Mechanisms of the Oxygen Evolution Reaction in RuO_2 and IrO_2. *ACS Catal.* **2020,** *10,* 3650-3657.

8. Chen, G. Z.; Lu, R. H.; Ma, C.; Zhang, X. W.; Wang, Z. Y.; Xiong, Y.; Han, Y, H. A Long-Range Disordering RuO_2 Catalyst for Highly Efficient Acidic Oxygen Evolution Electrocatalysis. *Angew. Chem. Int. Ed.* **2024,** 202411603.

9. Hong, W. T.; Risch, M.; Stoerzinger, K. A.; Grimaud, A.; Suntivich, J.; Shao-Horn, Y. Toward the Rational Design of Non-Precious Transition Metal Oxides for Oxygen Electrocatalysis. *Energy Environ. Sci.* **2015,** *8,* 1404-1427.

10. Feng, C.; Faheem, M. B.; Fu, J.; Xiao, Y. Q.; Li, C. L.; Li, Y. B. Fe-Based Electrocatalysts for Oxygen Evolution Reaction: Progress and Perspectives. *ACS Catal.* **2022,** *10,* 4019-4047.

11. Li. S. S.; Hao, X. G.; Abudula, A.; Guan, G. Q. Nanostructured Co-based Bifunctional Electrocatalysts for Energy Conversion and Storage: Current Status and Perspectives. *J. Mater. Chem. A* **2019,** *7,* 18674-18707.

12. Li, S. R.; Cong, J. L. Strategies for Improving the Performance and Stability of Ni-based Catalysts for Reforming Reactions. *Chem. Soc. Rev.* **2014,** *43,* 7245.

13. Song, H. J.; Yoon, H.; Ju, B.; Kim, D. W. Highly Efficient Perovskite Based Electrocatalysts for Water Oxidation in Acidic Environments: A Mini Review. *Adv. Energy Mater.* **2021,** *11,* 2002428.

14. Sun, C.W.; Alonso, J. A.; Bian, J. J. Recent Advances in Perovskite-Type Oxides for Energy Conversion and Storage Applications. *Adv. Energy Mater.* **2020,** *11,* 2000459.

15. Zhu, Y. L.; Zhou, W.; Yu, J.; Chen, Y. B.; Liu, M. L.; Shao, Z. P. Enhancing Electrocatalytic Activity of Perovskite Oxides by Tuning Cation Deficiency for Oxygen Reduction and Evolution Reactions. *Chem. Mater.* **2016,** *28,* 1691-1697.

16. Petrie, J. R.; Cooper, V. R.; Freeland, J. W.; Meyer, T. L.; Zhang, Z.; Lutterman, D. A.; Lee, H. N. Enhanced Bifunctional Oxygen Catalysis in Strained LaNiO$_3$ Perovskites. *J. Am. Chem. Soc.* **2016,** *138,* 2488–2491.

17. Liu, J. S.; Jia, E. D.; Stoerzinger, K. A.; Wang, L.; Wang, Y. N.; Yang, Z. Z.; Shen, D. W.; Engelhard, M. H.; Bowden, M. E.; Zhu, Z. H.; Chambers, S. A.; Du, Y. G. Dynamic Lattice Oxygen Participation on Perovskite LaNiO$_3$ during Oxygen Evolution Reaction. *J. Phys. Chem. C* **2020,** *124,* 15386-15390.

18. Retuerto, M.; Pereira, A. G.; Perez-Alonso, F. J.; Pena, M. A.; Fierro, J. L. G.; Alonso, J. A.; Fernandez-Diaz, M. T.; Pascual, L.; Rojas, S. Structural Effects of LaNiO$_3$ as Electrocatalyst for the Oxygen Reduction Reaction. *Appl. Catal. B-Environ.* **2017**, *203,* 363-371.

19. Hardin, W. G.; Slanac, D. A.; Wang, X. Q.; Dai, S.; Johnston, K. P.; Stevenson, K. J. Highly Active, Nonprecious Metal Perovskite Electrocatalysts for Bifunctional Metal–Air Battery Electrodes. *J. Phys. Chem. Lett.* **2013,** *4,* 1254–1259.

20. Guo, Q.; Li, X.; Wei, H. F.; Liu, Y.; Li, L. L.; Yang, X. J.; Zhang, X. H.; Liu, H.; Lu, Z. M. Sr, Fe Co-doped Perovskite Oxides with High Performance for Oxygen Evolution Reaction. *Front. Chem.* **2019,** *7,* 224.

21. Anjeline, C. J.; Marate, B. G.; Velu, D.; Kumar, S. M. S.; Lakshminarasimhan, N. Probing Oxygen Vacancy-induced Mixed-valence States of Nickel in LaNiO$_3$ and Their Influence on Electrocatalytic and Magnetic Properties. *Mater. Chem. Phy.* **2022,** *288,* 126331.

22. Choi, M. J.; Kim, T. L.; Kim, J. K.; Lee, T. H.; Lee, S. A.; Kim, C.; Hong, K.; Park, C. W.; Ko, K. T.; Jang, H. W. Enhanced Oxygen Evolution Electrocatalysis in Strained A-Site Cation Deficient LaNiO$_3$ Perovskite Thin Films. *Nano Lett.* **2020,** *20,* 8040-8045.

23. Arandiyan, J. H.; Mofarah, S. S.; Wang, Y.; Cazorla, C.; Jampaiah, D.; Garbrecht, M.; Wilson, K.; Lee, A. F.; Zhao, C.; Maschmeyer, T. Impact of Surface Defects on LaNiO$_3$ Perovskite Electrocatalysts for the Oxygen Evolution Reaction. *Chem. Eur. J.* **2021,** *27,* 14418-14426.

24. Sun, Y.; Li, R.; Chen, X. X.; Wu, J.; Xie, Y.; Wang, X.; Ma, K. K.; Wang, L.; Zhang, Z.; Liao, Q. L.; Kang, Z.; Zhang, Y. A-Site Management Prompts the Dynamic Reconstructed Active Phase of Perovskite Oxide OER Catalysts. *Adv. Energy Mater.* **2021,** *11,* 2003755.

25. Choi, S, B.; Kim, S. J.; Han, S.; Wang, J.; Kim, J.; Koo, B.; Ryabin, A. A.; Kunze, S.; Hyun, H.; Han, J.; Haw, S. C.; Chae, K. H.; Choi, C. H.; Kim, H.; Lim, J. Enhancing Oxygen Evolution Reaction via a Surface Reconstruction-Induced Lattice Oxygen Mechanism. *ACS Catal.* **2024,** *14,* 15096−15107.

26. Wu, Y. H.; Janak, M.; Abdala, P. M.; Borca, C. N.; Wach, A.; Kierzkowska, A.; Donat, F.; Huthwelker, T.; Kuznetsov, D. A.; Muller, C. R. Probing Surface Transformations of Lanthanum Nickelate Electrocatalysts during Oxygen

Evolution Reaction. *J. Am. Chem. Soc.* **2024,** *146,* 11887−11896.

27. Zhang, J.; Ye, Y.; Wei, B.; Hu, F.; Sui, L. T.; Xiao, H. W.; Gui, L. Q.; Sun, J.; He, B. B.; Zhao, L. Unveiling Anion Induced Surface Reconstruction of Perovskite Oxide for Efficient Water Oxidation. *Appl. Catal. B-Environ.* **2023,** *330,* 122661.

28. Chao, Y.; Ke, W. X.; Zhou, W. Y.; Cui, Y.; Lim, J. B.; Liang, P.; He, X.; Zhang, C. Constructing $LaNiO_3$/NiO Heterostructure via Selective Dissolution of Asite Cations from $La_{1-x}Sr_xNiO_3$ for Promoting Oxygen Evolution Reaction. *J. Alloy. Compd.* **2023,** *941,* 168908.

29. Liu, H.; Xie, R. R.; Wang, Q. X.; Han, J. L.; Han, Y.; Wang, J.; Fang, H.; Qi, J.; Ding, M.; Ji, W. X.; He, B.; Lu, W. M. Enhanced OER Performance and Dynamic Transition of Surface Reconstruction in $LaNiO_3$ Thin Films with Nanoparticles Decoration. *Adv. Sci.* **2023,** *10,* 2207128.

30. Sun, Y. Wu, C. R.; Ding, T. Y.; Gu, J.; Yan, J. W.; Cheng, J.; Zhang, K. H. L. Direct Observation of the Dynamic Reconstructed Active Phase of Perovskite $LaNiO_3$ for the Oxygen-Evolution Reaction. *Chem. Sci.* **2023,** *14,* 5906-5911.

31. Counsell, J. D. P.; Shard, A. G.; Cant, D. J.; Blomfied, C. J.; Navabpour, P.; Zhang, X. L. Gold, Silver, and Copper Reference spectra for XPS Instruments with Monochromatic Ag L_α Sources. *Surf. Sci. Spectra.* **2021,** *28,* 2.

32. Wei, C.; Sun, S. N.; Mandle, D.; Wang, X.; Qiao, S. Z.; Xu, Z. C. J. Approaches for Measuring the Surface Areas of Metal Oxide Electrocatalysts for Determining Their Intrinsic Electrocatalytic Activity. *Chem. Soc. Rev.* **2019,** *48,* 2518-2534.

33. Tyunina, M.; Peräntie, J.; Kocourek, T.; Saukko, S.; Jantunen, H.; Jelinek, M.; Dejneka, A. Oxygen Vacancy Dipoles in Strained Epitaxial $BaTiO_3$ Films. *Phys. Rev. Res.* **2020,** *2,* 023056.

34. Shan, F. K.; Liu, G. X.; Lee, W. J.; Shin, B. C. The Role of Oxygen Vacancies in Epitaxial-deposited ZnO Thin Films. *J. Appl. Phys.* **2007,** *101,* 053106.

35. Marco, J. F.; Gancedo, J. R.; Ortiz, J.; Gautier, J. L. Characterization of the Spinel-Related Oxides $Ni_xCo_{3-x}O_4$ (x = 0.3,1.3,1.8) Prepared by Spray Pyrolysis at 350 °C. *Appl. Surf. Sci.* **2004,** *227,* 175-186.

36. Qiao, L.; Bi, X. F.; Direct observation of Ni^{3+} and Ni^{2+} in correlated $LaNiO_{3-\delta}$ films, *Europhys. Lett.* **2011,** *93,* 57002.

37. Mickevicius, S.; Grebinskij, S.; Bondarenka, V.; Vengalis, B.; Sliuzien, K.; Orlowski, B. A.; Osinniy, V.; Drub, W. Investigation of Epitaxial $LaNiO_{3-x}$ Thin Films by High-Energy XPS. *J. Alloy. Compd.* **2006,** *423,* 107-111.

38. Alexander, M. R.; Thompson, G. E.; Beamson, G. Characterization of the Oxide/Hydroxide Surface of Aluminium Using X-ray Photoelectron Spectroscopy: A Procedure for Curve Fitting the O 1s Core Level. *Surf. Interface Anal.* **2000,** *29,* 468-477.

39. Trotochaud, L.; Young, S. L; Ranney, J. K.; Boettcher, S. W. Nickel-Iron Oxyhydroxide Oxygen-Evolution Electrocatalysts: The Role of Intentional and Incidental Iron Incorporation. *J. Am. Chem. Soc.* **2014,** *136,* 6744−6753.